Resonant two-photon spectroscopy of the 2s3d $^{1}D_{2}$ level of neutral ^{9}Be

E. C. Cook, A. D. Vira, and W. D. Williams

Resonant two-photon spectroscopy of the $2s3d\,^1D_2$ level of neutral ^{9}Be

E.C. Cook,[1] A.D. Vira,[1,2] and W.D. Williams[1,*]

[1]*Physics Department, Smith College, Northampton, MA 01063, USA*

[2]*Los Alamos National Laboratory, Los Alamos, NM, 87545, USA*

(Dated: March 9, 2020)

Abstract

We report an absolute frequency measurement of the $2s3d\,^1D_2$ state in neutral beryllium-9 using two-photon spectroscopy with a resonant intermediate state. The absolute center-of-gravity energy is determined to be $64\,428.40321(55)$ cm^{-1}, a factor of 180 more precise than the previous experimental measurement. We also confirm our previous result for the energy of the intermediate $2s2p\,^1P_1$ level. Precision is limited by unresolved hyperfine structure and the complications of performing resonant two-photon spectroscopy on an atomic beam. A three-level rate-equation analysis is presented to explore, and minimize, systematic uncertainties arising from small atomic/optical beam angle deviations from perpendicular.

---
[*] wwilliams@smith.edu

I. INTRODUCTION

Precision spectroscopy of the light elements serves an important role in aiding and refining theoretical methods of atomic structure calculation. While the theoretical precision for beryllium still lags behind the other light elements, recent improvements in theoretical models have resulted in predictions for several energy levels that exceed current experimental results [1–3]. Measurements of the $2s^2\,{}^1S_0 - 2s2p\,{}^1P_1$ transition energy and ionization threshold of neutral ^{9}Be hold particular interest in serving as tests of the latest nonrelativistic wavefunction calculation methods and incorporation of leading relativistic and quantum-electrodynamic (QED) corrections. Puchalski *et al.*, using explicitly correlated Gaussian (ECG) basis sets while taking into account relativistic, QED, and finite nuclear mass effects, calculated the $2s^2\,{}^1S_0 - 2s2p\,{}^1P_1$ transition energy to be $42\,565.441(11)$ cm^{-1} [1], with a QED shift of $1.048(9)$ cm^{-1}, a prediction verified by our recent saturated absorption measurements of this transition which found $42\,565.4501(13)$ cm^{-1} [4].

Two-photon spectroscopy of the $2s3d\,{}^1D_2$ state using the $2s2p\,{}^1P_1$ state as a resonant intermediate state offers an alternative verification of the $2s^2\,{}^1S_0 - 2s2p\,{}^1P_1$ transition energy. A measurement of the ionization threshold, which would be a test of QED, using Rydberg spectroscopy from the $2s3d\,{}^1D_2$ state to the $2snp\,{}^1P$ states also requires an absolute frequency measurement of the $2s3d\,{}^1D_2$ state.

Other recent theoretical interest in beryllium includes calculations of the nonrelativistic energy for the ground state using the Hylleraas-configuration-interaction (Hy-CI) method, which reached 10 nanohartree precision [5], calculation of a large number of energy levels for both singlet and triplet excited states to millihartree precision [6, 7], the total and transition energies of the four lowest ${}^1S$ states using ECG with relativistic and QED corrections [3], and isotope shift calculations using ECG with relativistic and QED corrections [8]. The calculations of Ref. [8] call for isotope shift measurements on neutral beryllium isotopes to confirm nuclear charge radii results obtained from spectroscopic measurements on the beryllium ion [9] in combination with the previously-measured ^{9}Be nuclear charge radius [10]. The absolute energy of the $2s3d\,{}^1D_2$ state, which is the focus of this work, was calculated by Sharkey *et al.* using ECG, but not including relativistic or QED corrections, to be $64\,418.17(5)$ cm^{-1} [11]. Since this calculation does not yet include higher-order corrections, it cannot be directly compared to our experimental result. However, our result

provides motivation to include these corrections as a test of both the theoretical methods and QED.

Many of the most precise experimental measurements of the energy levels of neutral ^{9}Be occurred over 50 years ago. In 1953, Bozman *et al.* [12] measured the $2s^2\,^1S_0 - 2s2p\,^3P_1$ transition to have energy $21\,978.925(10)$ cm^{-1}. In 1962, Johansson performed measurements of many transitions with 0.01-0.02 Å precision [13]; the $2s^2\,^1S_0 - 2s2p\,^1P_1$ and $2s2p\,^1P_1 - 2s3d\,^1D_2$ transition energies were measured to be $42\,565.35(18)$ cm^{-1} and $21\,862.96(05)$ cm^{-1}, respectively. In 1983, Beigang *et al.* improved upon the work of Seaton by determining the ionization potential of beryllium to be $75\,192.64(6)$ cm^{-1} [14, 15]. Relevant to this work, the absolute energy of the $2s3d\,^1D_2$ state was measured by Johansson to be $64\,428.31(10)$ cm^{-1} [13, 16]. The work presented here is in agreement with and a factor of 180 more precise than the previous experimental result.

In this work, we perform two-photon spectroscopy on the $2s^2\,^1S_0 - 2s3d\,^1D_2$ transition in neutral ^{9}Be, using the $2s2p\,^1P_1$ level as a resonant intermediate state; for the rest of the paper, we will refer to these states as the $^1S_0$, $^1P_1$, and $^1D_2$ states. The lasers are referenced to a temperature-stabilized ultra-low expansion cavity calibrated using a femtosecond frequency comb, for absolute laser frequency determination better than ± 110 kHz. The use of a resonant intermediate state allows direct absorption detection of the $^1P_1 - {}^1D_2$ resonance and independent verification of the $^1S_0 - {}^1P_1$ transition energy. However, imperfect perpendicularity of the optical and atomic beam axes imposes a systematic frequency shift not present in resonant two-photon spectroscopy on an isotropic velocity distribution. Additional uncertainty in center-of-gravity transition energy determination is introduced by the merged hyperfine spectral features of both transitions.

In Sec. II, we present a simplified model that reproduces the systematic shifts arising in resonant two-photon spectroscopy addressing the anisotropic velocity distribution of a hot atomic beam and provides guidance for the experimental procedure. Section III describes the experimental spectroscopy and laser frequency calibration setup, and Sec. IV presents results and a discussion of the other systematic and statistical uncertainties that limit the precision of this experiment. Section V concludes with a summary of the results and suggestions for future experiments.
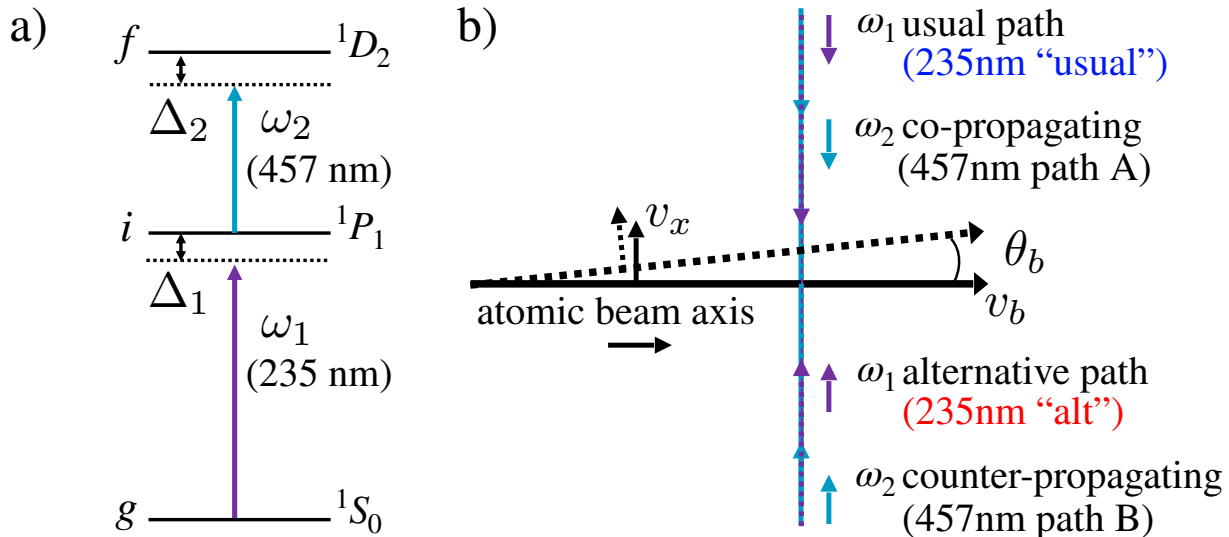
FIG. 1: a) Three-level system interacting with two laser fields. b) Simplified experimental setup to illustrate two-photon optical axis configuration perpendicular to the atomic beam axis, probing a cold gas distribution, vs. off-perpendicular by an angle θ_b. Here co-/counter-propagating are defined with respect to the ω_1 usual path; reversing the direction of ω_1 to use the alternative path reverses the sign of the optical/atomic beam angle θ_b.

II. BACKGROUND

The use of a resonant intermediate state in two-photon spectroscopy (also called two-step spectroscopy) offers a signal enhancement effect dominated by velocity selection of atoms promoted to the intermediate state. As a result, the Doppler shifts arising in resonant two-photon spectroscopy performed using an atomic beam (or any other anisotropic velocity distribution) can lead to systematic frequency shifts not observed in isotropic velocity distributions, such as a vapor cell.

To investigate this systematic, we follow the formalism of Bjorkholm and Liao [17] for a simplified three-level system, ignoring hyperfine substructure (see Fig. 1a). Resonant two-photon spectroscopy is well-described in the low-intensity limit by a rate-equation approach: for a three-level system addressed by two laser fields $\omega_1 = k_1 c$ (detuned by $\Delta_1 = \omega_{ig} - \omega_1$ from the ground to intermediate transition) and $\omega_2 = k_2 c$ (detuned by $\Delta_2 = \omega_{fi} - \omega_2$ from the intermediate to final transition), the upper-level absorption can be shown to be equivalent to the overall transition rate

$$R_{2\gamma}(\Delta_2) = \frac{\Omega_1^2\,\Omega_2^2\,\Gamma_f}{\left(\Delta_1 - \boldsymbol{k_1}\cdot\boldsymbol{v}\right)^2 + \left(\Gamma_i/2\right)^2}$$

$$\times \frac{1}{\left(\Delta_1 + \Delta_2 - (\boldsymbol{k_1} + \epsilon\boldsymbol{k_2})\cdot\boldsymbol{v}\right)^2 + \left(\Gamma_f/2\right)^2}, \tag{1}$$

where $\Omega_{1(2)}$ is the Rabi frequency characterizing the strength of the electric field coupling the ground to intermediate (intermediate to final) states, $\Gamma_{i(f)}$ is the decay rate of the intermediate (final) state, and $\epsilon = +/-1$ for co-/counter-propagating wavevectors $\boldsymbol{k_1}$ and $\boldsymbol{k_2}$.

To calculate the two-photon lineshape, or the absorption rate as a function of Δ_2 for a given detuning Δ_1, this expression is integrated over the velocity distribution addressed by the two laser fields. The denominator of the first term in this expression accounts for the velocity-selective behavior of near-resonant two-photon excitation, or the dependence of the intermediate state population on the detuning of ω_1 when Δ_1 is on the order of or smaller than the Doppler width $\Gamma_D = (\omega_{ig}/c)\sqrt{8\ln 2\,k_B T/m}$ of the intermediate level. In the large-detuning or virtual-intermediate-state limit $\Delta_1 \gg \Gamma_D$, step-wise excitation to the intermediate state is negligible. In this case, the resonance condition, or the value of Δ_2 giving peak absorption for a given Δ_1, reduces to the energy-conservation condition $\Delta_2 = -\Delta_1$. As the detuning decreases the absorption of ω_2 is dominated by the ability of ω_1 to populate the intermediate state. For detunings $\Delta_1 \ll \Gamma_D$ we might expect the resonance condition to depend only upon the respective Doppler shifts of the two beams, such that $\Delta_2 = \epsilon\,(k_2/k_1)\Delta_1$. However, as the sampled gas becomes colder and Γ_D decreases, the intermediate state population is heavily weighted by the relative shift of the available thermal distribution, and the slopes of the co- and counter-propagating resonance curves decrease and increase, respectively, as illustrated in Fig. 2. For both a hot and a cold gas, the co- and counter-propagating resonance curves cross at $\Delta_1 = \Delta_2 = 0$.

An anisotropic velocity distribution, such as an atomic beam, can have a complex angular distribution dependent on oven temperature and beam collimation characteristics. As a simplified model, the transverse distribution (perpendicular to the atomic beam axis) can be assumed $\sim \mathrm{Exp}[-v_x^2 M/(2k_B T_g)]$, characteristic of a cold gas at temperature T_g. However, the longitudinal distribution will be characterized by the hot beam temperature T_b and will take a form similar to $v_b^2\,\mathrm{Exp}[-v_b^2 M/(2k_B T_b)]$ [18]. In this case, the Doppler shift terms $\boldsymbol{k}\cdot\boldsymbol{v}$
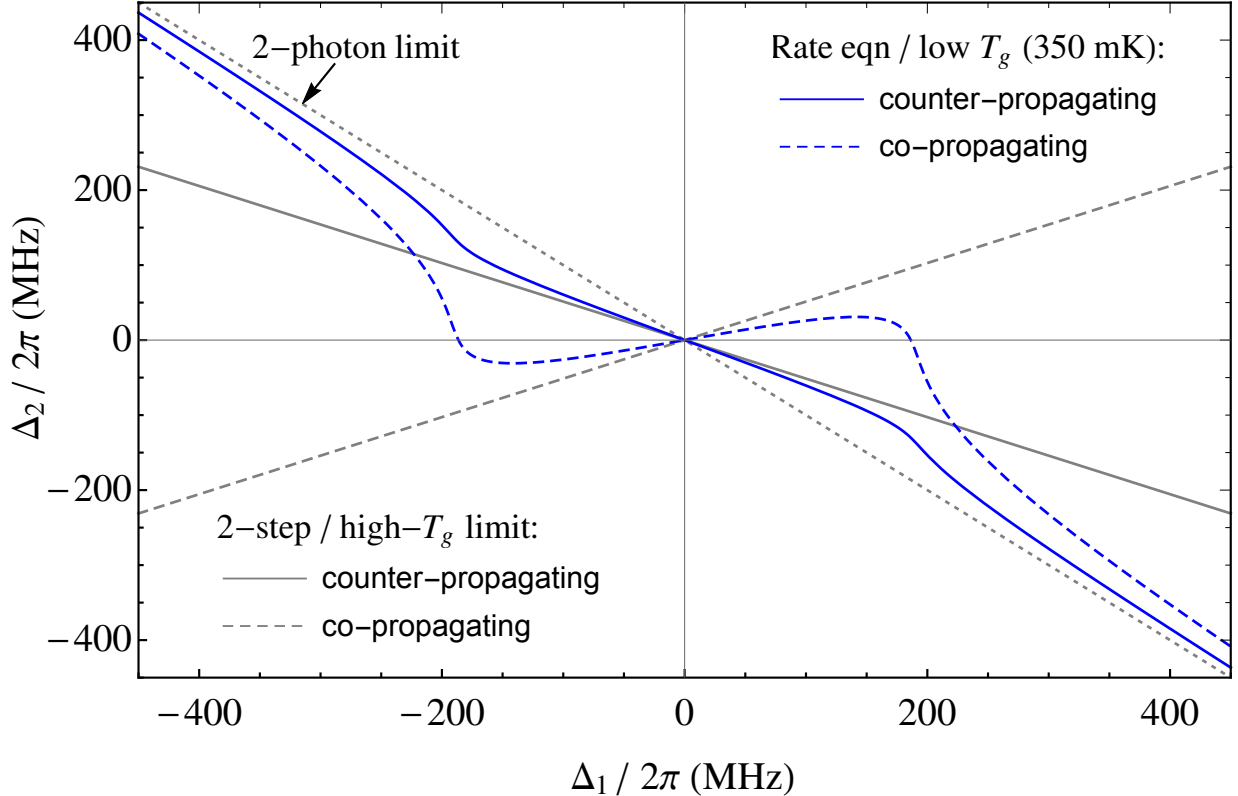
FIG. 2: Theoretical resonance conditions (value of Δ_2 giving peak absorption for a given Δ_1) in an isotropic velocity distribution. Shown in the figure are the virtual (non-resonant) 2-photon limit (dotted gray), resonant 2-step excitation limit in a hot gas (solid/dashed gray), and the result of the rate-equation model for a 3-level atom whose properties are taken from the ^{9}Be $^1S_0 - {}^1P_1 - {}^1D_2$ 2-step transition in a relatively cold (T_g=0.35 K, $\Gamma_D/2\pi$=180 MHz) isotropic gas (blue).

in Eq. 1 contain both longitudinal and transverse velocity components and derivation of the two-photon spectrum requires integration over both distributions.

As illustrated in Fig. 1b, when the optical and atomic beam axes are off-perpendicular by an angle θ_b,

$$\boldsymbol{k} \cdot \boldsymbol{v} = k v_x \cos \theta_b + k v_b \sin \theta_b. \tag{2}$$

The co- and counter-propagating resonance curves shift such that the crossing point is no longer $\Delta_1 = \Delta_2 = 0$. The crossing-point shift is reversed, however, by reversing the sign of θ_b, which is equivalent to bringing the ω_1 beam in from the opposite direction (ω_1 alternative path in Fig. 1b). Figure 3 illustrates this effect for $\theta_b = \pm 3$ mrad, $T_g = 0.35$ K, and $T_b = 1473$ K for a 3-level atom whose properties are taken from the ^{9}Be

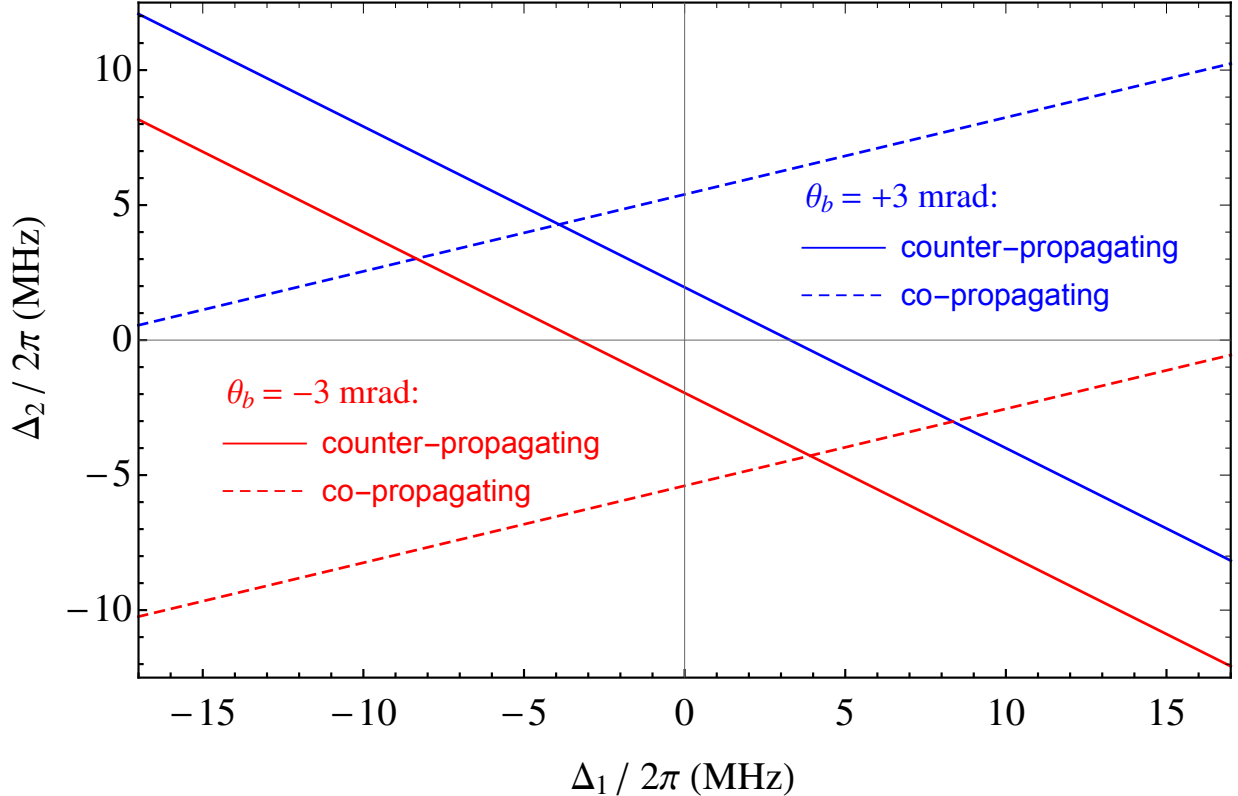FIG. 3: Theoretical resonance conditions (value of Δ_2 giving peak absorption for a given Δ_1) in an anisotropic velocity distribution for optical axes off-perpendicular to the atomic beam axis by $\theta_b = \pm 3$ mrad (result of rate-equation model for a 3-level atom whose properties are taken from the ^{9}Be $^1S_0 - {}^1P_1 - {}^1D_2$ 2-step transition with $T_g = 0.35$ K and $T_b = 1473$ K).

$^1S_0 - {}^1P_1 - {}^1D_2$ transition. The slopes of the co-/counter-propagating resonance curves and the magnitude of the crossing-point shift is heavily dependent on the precise form and characteristic temperatures of the transverse cold gas and longitudinal hot atomic beam velocity distributions, as well as θ_b. However, the co-/counter-propagating crossing points for the configurations with $\pm\theta_b$ remain symmetric about $\Delta_1 = \Delta_2 = 0$ across variations of these parameters.

The systematic shift resulting from imperfect perpendicularity of the optical/atomic beam axes can therefore be accounted for by deriving resonance curves from the co- and counter-propagating spectra in both configurations; $\Delta_1 = \Delta_2 = 0$ is then determined from the midpoint of the crossing points of the two configurations. This insight guides the experimental procedure. Each resonant condition, as explained above, is found using each possible
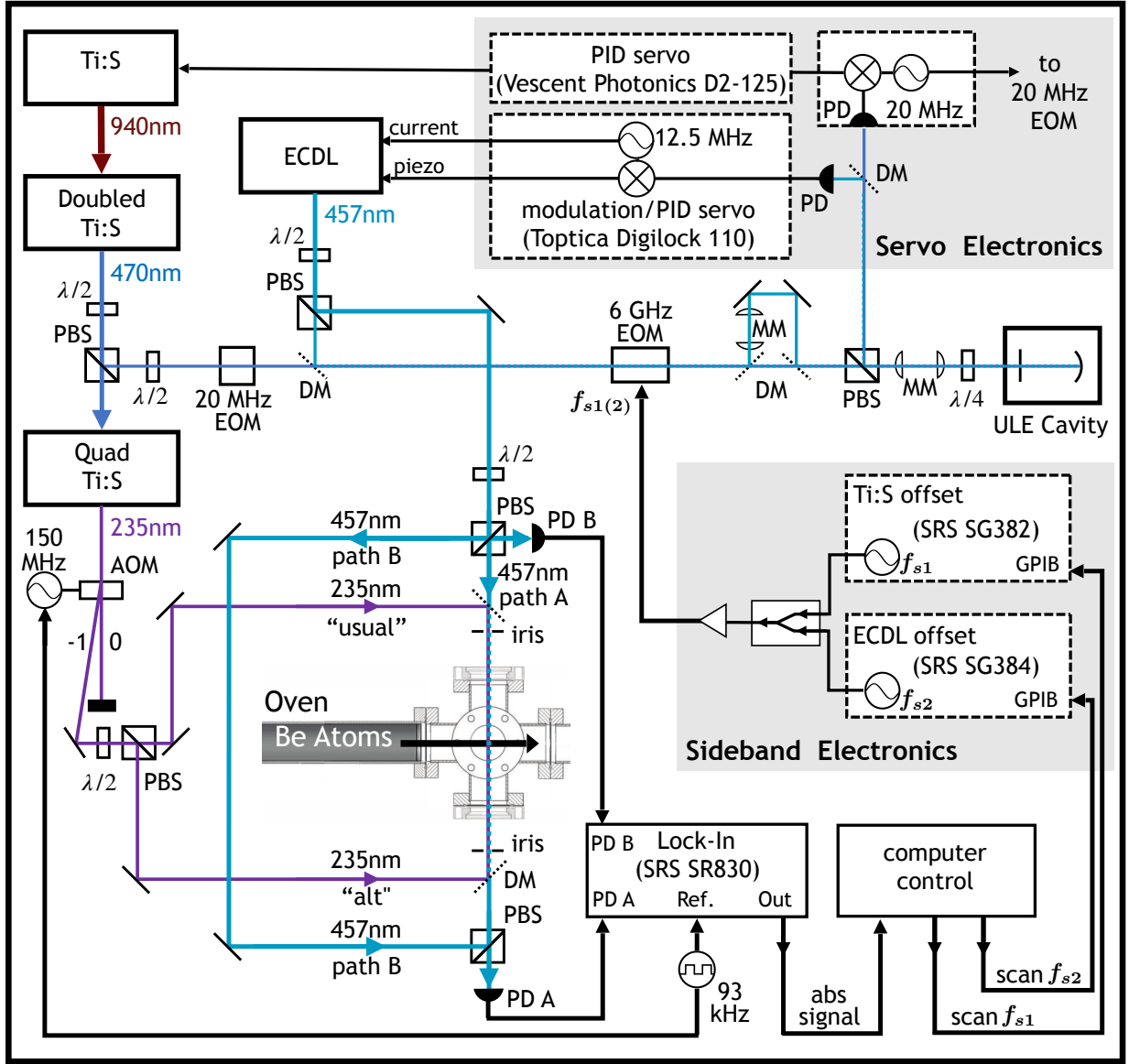
FIG. 4: Simplified experimental setup for laser stabilization and two-photon absorption spectroscopy. (MM: mode-matching lenses; DM: dichroic mirror)

combination of ω_1 and ω_2 as shown in Fig. 1b. The off-axis systematic is eliminated by taking the midpoint value of the usual/alt configuration co-/counter-propagating cross points, as illustrated in Fig. 3.

III.   EXPERIMENTAL SETUP

Figure 4 shows the experimental setup for the two-step absorption measurement. We use a commercial oven at $1200°$C to produce a collimated beryllium beam with a transverse temperature less than 1 K, as described in [4], and a frequency-quadrupled Ti:Sapphire (Ti:S) laser (MSquared Lasers) to address the $^1S_0 - {}^1P_1$ transition at 234.9 nm. A Toptica Photonics external cavity diode laser (ECDL) at 457.4 nm is used to address the $^1P_1 - {}^1D_2$ transition. The 235 nm light passes through a 150 MHz acousto-optic modulator (AOM) chopped at 93 kHz; the negative 1st-order beam then splits at a polarizing beam-splitter (PBS) to provide equal-length paths ("usual" vs "alt") to address the atomic beam from either side of the vacuum chamber with roughly collimated $1/e^2$ horizontal×vertical beam waists of $0.9(1)×1.4(1)$ mm. The 457 nm experiment path is likewise roughly collimated and split into paths A and B, co-propagating with the 235 nm "usual" and "alt" paths, respectively, with $1/e^2$ horizontal×vertical beam waists of $1.4(1)×1.0(1)$ mm $(1.9(1)×1.7(1)$ mm) at the atomic beam along path A(B). At the vacuum chamber, we align through two iris diaphragms with 1 mm apertures and a 72 cm separation distance for a 457/235 nm overlap angle uncertainty better than 1.5 mrad; the irises also set the limit on our ability to reverse beam directions for the usual/alt configuration measurements. For equal intensities, the power of path B is adjusted to be $2.2×$ the power of path A. Photodectors (PD A/B, Thorlabs PDA36A) monitor the transmission of the 457 nm beams, with the outputs demodulated at the 235 nm AOM chop frequency.

As in Ref. [4], we reference the frequency-doubled output of the Ti:S at 470 nm to a calibrated, temperature-stabilized ultralow-expansion (ULE) cavity [19] using an offset sideband lock [20]; in this experiment, the 457 nm light is simultaneously referenced to the same ULE cavity. The 470 nm beam passes through a 20 MHz electro-optic modulator (EOM) followed by a temperature-stabilized high-frequency fiber EOM before mode-matching into the ULE cavity. The ECDL providing the 457 nm light is current-modulated at 12.5 MHz and joins the 470 nm beam path through the fiber EOM at a dichroic mirror; after the fiber EOM the 457 nm path splits at another dichroic for independent mode-matching before recombining into the ULE cavity. The light reflected from the cavity is split using a final dichroic and sent to separate photodiodes, allowing independent demodulation of the 470 nm and 457 nm signals at 20 MHz and 12.5 MHz, respectively, to produce standard Pound-Drever-

Hall (PDH) error signals for laser stabilization [21]. The 470 nm signal is processed by a commercial photodetector/demodulation unit (Stable Laser Systems PDH-1000-20B) with a Vescent servo (D2-125-PL) for feedback to the Ti:S external reference cavity. The 457 nm signal is detected by a fast photodiode (Thorlabs PDA10A) and demodulated using the Toptica Digilock 110 software for feedback to the ECDL current and piezo.

We drive the high-frequency fiber EOM with the combined outputs f_{s1} and f_{s2} of two RF signal generators (SRS SG384 and SG382) to allow calibrated, independent frequency scans of the two lasers. After the fiber EOM, each beam has high-frequency, tunable sidebands at both f_{s1} and f_{s2} in addition to the fixed 20 / 12.5 MHz modulation (as well as small features at $f_{s1} \pm f_{s2}$). Choosing the appropriate negative sideband to stabilize to the ULE cavity, the laser frequencies are given by

$$f_L = f_n + f_{\mathrm{EOM}}, \tag{3}$$

where f_n is the frequency of the lower ULE cavity mode and $f_{\mathrm{EOM}} = f_{s1(2)}$ for the 470 nm (457 nm) beams, such that $2f_{s1}$ controls the detuning of ω_1 at 235 nm and f_{s2} controls the detuning of ω_2 at 457 nm.

IV. RESULTS AND DISCUSSION

Co- and counter-propagating spectra are recorded from each side of the vacuum chamber (see Fig. 1b/Fig. 4) to account for imperfect perpendicularity between the optical and atomic beam axes, as described in Sec. II. For the "usual" 235 nm beam path, 457 nm path A is co-propagating and path B is counter-propagating, while the opposite is true for the "alt" 235nm beam path. With the lasers stabilized to the ULE cavity as described in Sec. III, we record the two-photon 457 nm absorption spectrum at fixed 235 nm detunings Δ_1 independently for each configuration, with the two other beams blocked to avoid saturation and optical pumping effects, by stepping sideband f_{s2} in 2 MHz increments to scan Δ_2 across the two-photon resonance. We average each data point for 100 ms, after 100 ms settling time, and alternately scan up and down in frequency to check for hysteresis effects; no hysteresis was observed. Each spectrum is then fit to a Lorentzian to determine the value f_{s2} of peak absorption (the resonance condition Δ_2 for the current value of Δ_1).

See Fig. 5 for examples of typical two-photon resonance spectra and corresponding fits
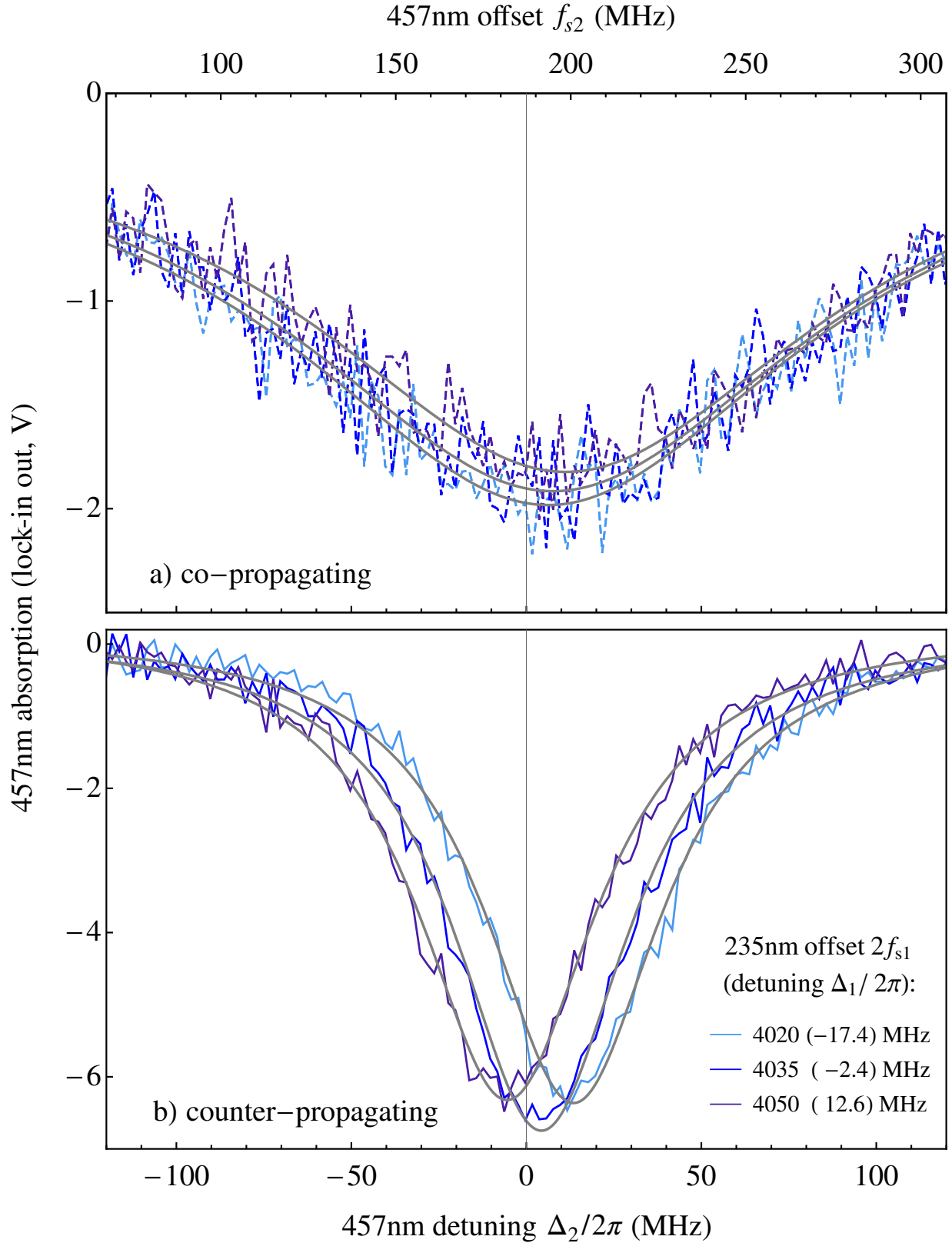
FIG. 5: Two-photon spectra (457 nm absorption signal demodulated at 235 nm chop frequency) and Lorentzian fits acquired for several 235 nm detunings at the second-to-lowest intensity level used ($P_{235} = 1.0$ mW), usual 235 nm path (457 nm path A: co-propagating, path B: counter-propagating). Detunings Δ_1 and Δ_2 are calibrated to the derived zero-intensity values; see text. The hyperfine structure is unresolved.
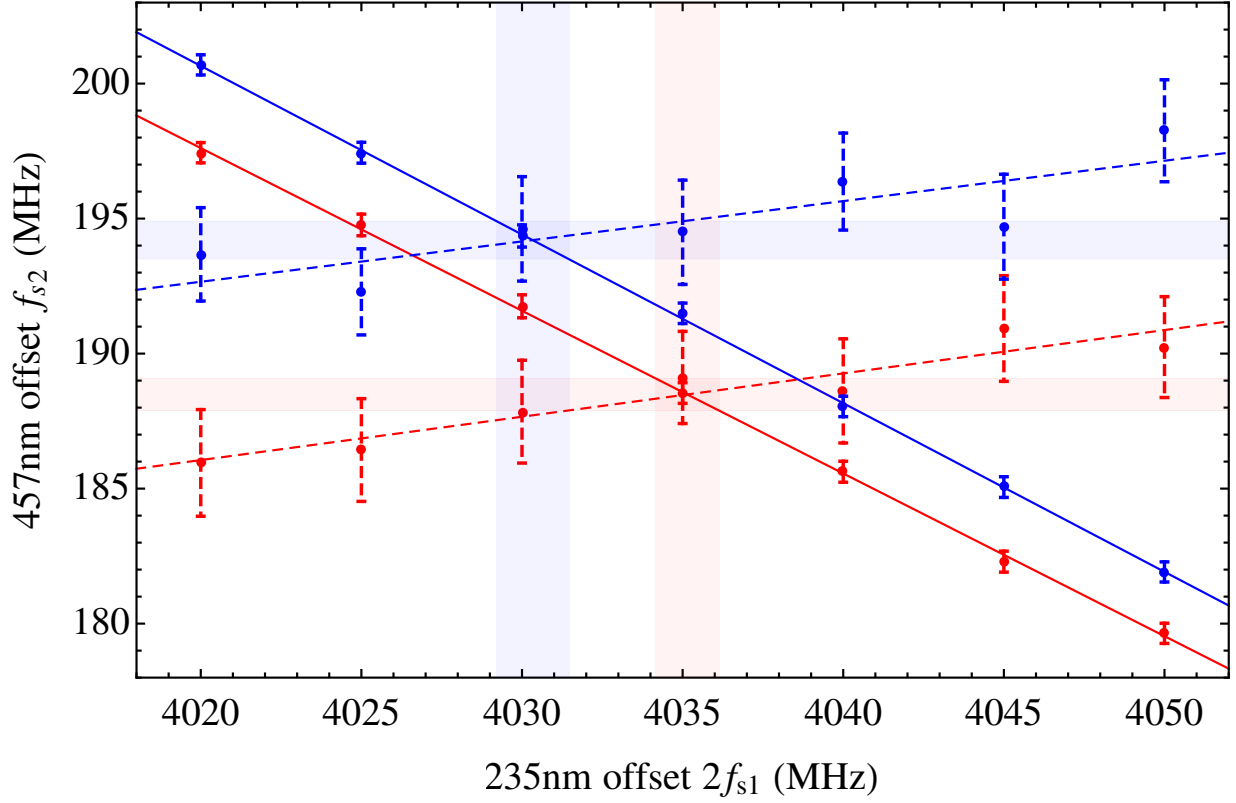
FIG. 6: Linear fit resonance conditions Δ_2 derived from fits to co-/counter-propagating spectra acquired at each Δ_1 for the usual (upper blue dashed/solid curves) and alt (lower red dashed/solid curves) configurations at the second-to-lowest intensity level used ($P_{235} = 1.0$ mW). Shaded blue/red regions indicate 1σ cross-point uncertainties for the usual / alt configurations. Similar curves are recorded at six power levels to account for intensity-dependent spectral shifts; see text for details.

recorded in the co- and counter-propagating geometries for the "usual" 235 nm beam path; frequency detunings for the 235 / 457 nm beams are given in both offset sideband lock frequencies $2f_{s1}/f_{s2}$ and Δ_1/ Δ_2 values calibrated to the derived zero-intensity values as described below. Due to hyperfine structure, the spectrum is actually a combination of multiple spectral lineshapes. However, for this analysis we are concerned with extracting the peak absorption, and spectral asymmetries not captured by the Lorentzian fit are reversed in the "alternative" configuration and thus cancel out of the final midpoint derivation. The unresolved hyperfine structure adds an overall uncertainty to our absolute frequency measurements that is addressed below.

We map out the resonance condition for each configuration by stepping the frequency of

the sideband f_{s1} generating the Ti:S error signal by 2.5 MHz (5 MHz at 235 nm), recording the 457 nm absorption spectrum, and determining the peak f_{s2} absorption point at seven to eleven 235 nm detunings. The co-/counter-propagating resonance curve crossing points are determined from the crossing points of linear least-squares fits to each data set with weighting equal to the square inverse of the data point uncertainties. Figure 6 shows typical usual and alt configuration data sets and cross-point confidence intervals. As described in Sec. II, any misalignment of the optical/atomic beam axes off-perpendicular introduces frequency shifts in the crossing points observed in the usual versus alt configurations; the zero-atomic-beam-angle crossing point for these experimental parameters lies midway between the usual and alt configuration crossing points.

Full data sets must be recorded at several intensity levels to account for intensity-dependent spectral shifts. The rate-equation model of Sec. II is a low-intensity approximation; while 235 nm power levels can be kept well below the $^1S_0 - {}^1P_1$ saturation intensity ($I_{\mathrm{sat1}} = 886$ mW/cm^2), each resonant 235 nm photon absorption imparts a 457 nm recoil shift of +/- 413 kHz for the co-/counter-propagating geometries. Furthermore, the 457 nm intensities required for sufficient absorption signal strength are on the order of or greater than the $^1P_1 - {}^1D_2$ transition saturation intensity of $I_{\mathrm{sat2}} = 17$ mW/cm^2. A full accounting of the intensity-dependent shifts would require a density-matrix approach [22] incorporating as well the 235 nm recoil shifts and modification to the velocity distributions. For the precision of this experiment, it is sufficient to repeat each measurement at several power levels, increasing both the 235 and 457 nm intensities until the observed intensity-dependent shifts are outside the linear regime, and extrapolate to zero intensity.

We recorded full resonance curve data sets at six power levels, stepping the 235 nm power (P_{235}) recorded after the vacuum chamber in 0.5 mW increments from 0.5 - 3.0 mW while setting the 457 nm path A power to $0.5P_{235}$. We set the 457 nm path B power to an equivalent intensity, for full resonance curve data sets recorded at $I_{235} = (0.03 - 0.18) \times I_{\mathrm{sat1}}$ in $0.03\,I_{\mathrm{sat1}}$ increments and $I_{457} = (0.7 - 4.2) \times I_{\mathrm{sat2}}$ in $0.7\,I_{\mathrm{sat2}}$ increments. At each power level, we extract the usual/alt co-/counter-propagating resonance curve crossing points: see Fig. 7. Figure 8 plots the six usual/alt cross-points versus 235 nm power; for the four lowest power levels, the observed intensity-dependent shifts are sufficiently linear for the precision of this experiment.

The intercepts of weighted linear fits to the four lowest-power midpoints give the 235 nm
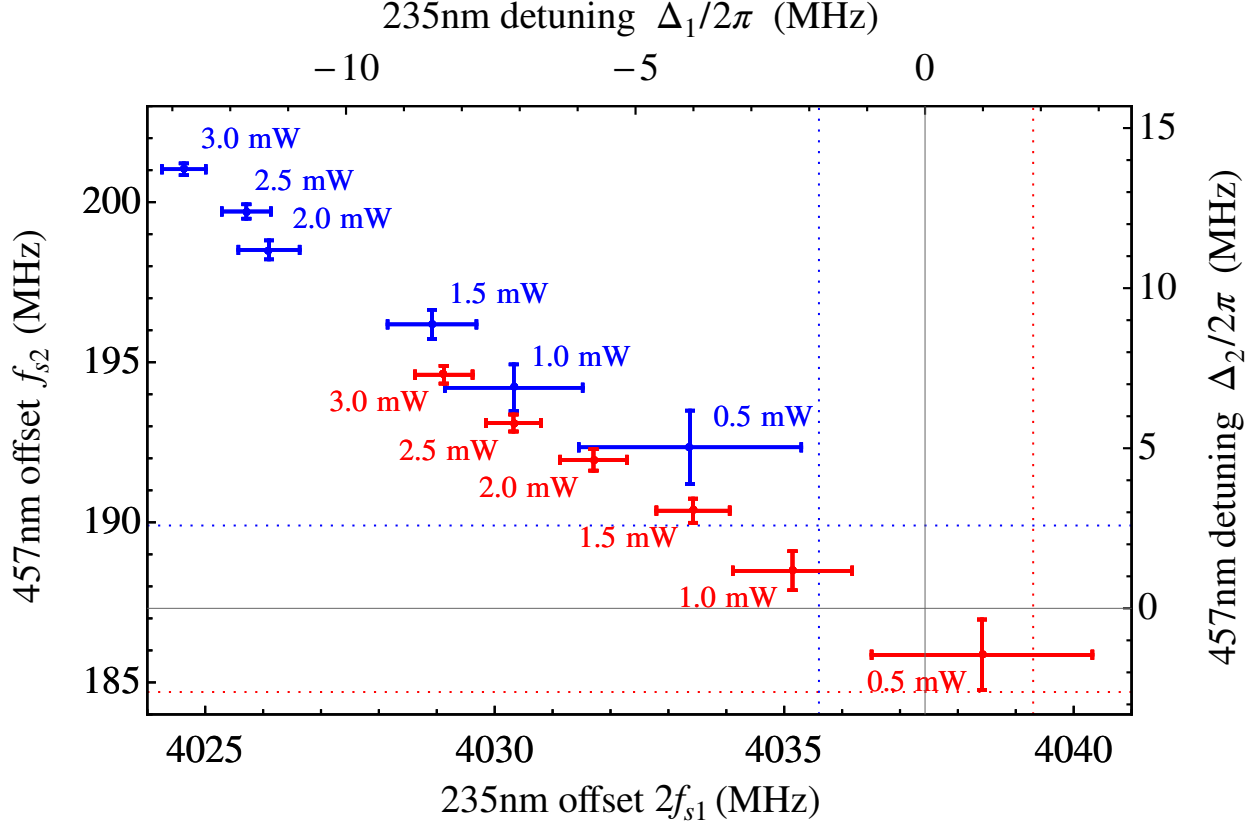
FIG. 7: Co-/counter-propagating cross points for the usual (blue) and alt (red) configurations at the six power levels described in the text. The zero-intensity linear-fit intercepts for the usual and alt configurations (see text) are marked by the blue and red dotted gridlines; detunings Δ_1 and Δ_2 are calibrated to the derived midpoint zero-intensity values.

and 457 nm offset frequencies corresponding to $\Delta_1 = \Delta_2 = 0$ as $2f_{s1}^0 = 4037.5(1.1)$ MHz and $f_{s2}^0 = 187.3(7)$ MHz, respectively. Alternatively, taking the midpoint of the intercepts of the usual/alt crossing point linear extrapolations gives an equivalent result within uncertainty. The linear least-squares fits are shown by dotted curves in Fig. 8; to verify the low-intensity assumption we also fit the cross points for all six power levels to a saturation model $\propto c^0 + I_{\rm tot}/(1 + I_{\rm tot})$, where $I_{\rm tot} \propto P_{235}$. The saturation model intercepts c^0 agree with the linear model intercepts within overall uncertainty.

Table I lists systematic and statistical uncertainties affecting our absolute frequency determinations. As described in Sec. III, the laser frequencies addressing the beryllium atoms are given by

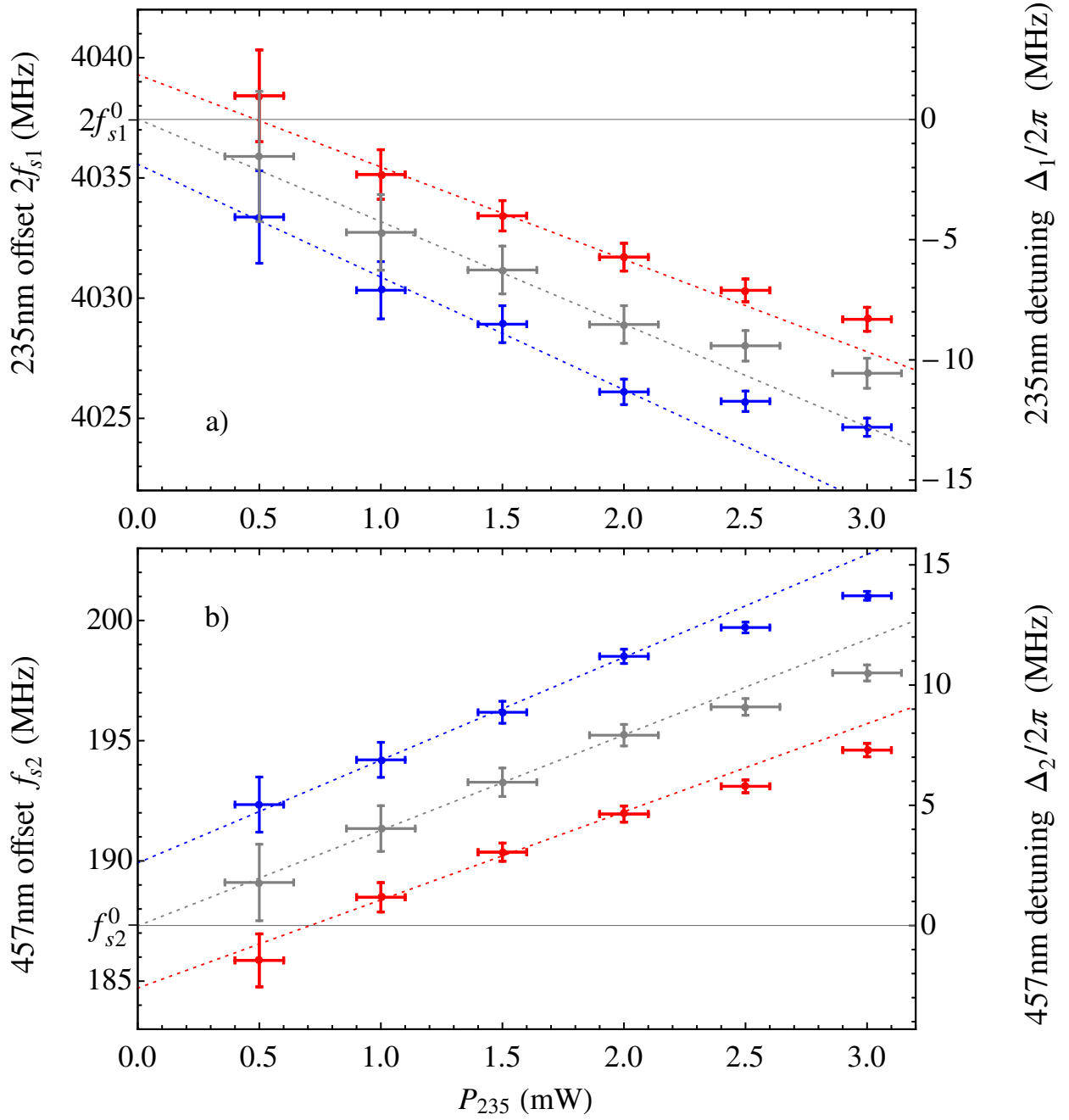$$f_2 = f_{n_2} + f_{s2} \tag{4}$$

14

FIG. 8: Cross-point intensity shifts: usual (blue), alt (red), and midpoints (gray). Linear least-squares fits (dotted) to the four lowest-intensity points are used to extrapolate the values a) $2f_{s1}^0$ corresponding to $\Delta_1 = 0$ and b) f_{s2}^0 corresponding to $\Delta_2 = 0$.

for the 457 nm beam (locked to ULE cavity mode f_{n_2} using the negative f_{s2} sideband of the high-frequency EOM) and

$$f_1 = 2(f_{n_1} + f_{s1}) + f_{\text{AOM}} \tag{5}$$

for the 235 nm beam (with the 470 nm output of the frequency-doubled Ti:S locked to ULE cavity mode f_{n1} using the negative f_{s1} sideband of the high-frequency EOM). The 235 nm beam is the frequency-quadrupled Ti:S output with an additional $f_{\text{AOM}} = -149.998(2)$ MHz shift, with the AOM frequency verified using a pickup coil and SRS SR620 counter. We measure the absolute frequency of cavity mode f_{n_1} to ± 24 kHz by beating the locked Ti:S output against the frequency-doubled output of a femtosecond comb (Toptica DFC CORE with doubler EXT935) referenced to a 10 MHz GPS-calibrated oscillator (Stanford Research Systems FS740), using a 30 MHz wavemeter (High-Finesse/Ångstrom WS7/30) to verify the comb order. Since the frequency comb measures wavelengths in the infared, we tune the Ti:S to 914 nm, stabilize the 457 nm frequency-doubled output to the ULE cavity, and repeat the procedure to measure f_{n_2}. We repeat the cavity mode calibration before and after final data collection, measuring a drift of < 33 kHz, and include a 35 kHz Pound-Drever-Hall (PDH) stabilization offset drift for the Ti:S (attributed to residual amplitude modulation in the 20 MHz EOM) and a 20 kHz PDH offset drift for the ECDL (attributed to amplitude modulation accompanying the 12.5 MHz ECDL current modulation). The combined absolute laser frequency uncertainty is 45 kHz at 457 nm and 110 kHz at 235 nm.

Determination of the absolute frequency of the observed $^1D_2$ spectral feature includes the 2 kHz AOM frequency drift for f_1 and the uncertainty of the f_{s2}^0 and $2f_{s1}^0$ values derived from the linear extrapolation to zero intensity as described above. We include an additional 6.6 MHz uncertainty from the 1.5 mrad optical beam angle tolerance, calculated from the 457 nm Doppler shift arising in a 1200°C beam. This systematic addresses both the 235/457 nm overlap tolerance and the reversibility of the the usual/alt configurations, and is verified by repeatability of resonance condition data sets.

We are further limited in determination of the $2s3d\,^1D_2$ center-of-gravity energy by the unresolved hyperfine structure, which is the dominate uncertainty of this measurement. Although resonant two-step spectroscopy can show the hyperfine structure of both the excited and intermediate states, our previous saturated absorption measurements of the $^1S_0 - {}^1P_1$ transition revealed merged spectra, indicating a hyperfine splitting smaller than the 88 MHz natural linewidth. Similarly, the expected 15 MHz hyperfine spread of the $^1D_2$ sublevels

TABLE I: Systematic and statistical measurement uncertainties (one standard deviation) for the absolute energy of the $2s3d\,^1D_2$ state.

Uncertainty contribution	f_1(kHz)	f_2(kHz)
ULE cavity mode calibration	2×24	24
Cavity mode drift	2×33	33
PDH offset drift	2×35	20
AOM frequency drift	2	–
Zero-intensity cross point	670	1 100
Optical beam overlap/reversibility angle	6 600	
Unresolved hyperfine structure	15 000	
Overall (quadrature sum)	**16 400 kHz**	
Overall in cm^{-1}	**0.00055 cm^{-1}**	

(from $F = 7/2$ to $F = 1/2$ using nuclear spin $I = 3/2$ and measured magnetic dipole constant $A = 4(1)$ MHz [23]) is on the order of the 12 MHz $^1P_1 - {}^1D_2$ natural linewidth. We do not see any evidence of hyperfine structure in our absorption spectra (see Fig. 5), and the linewidths of the single-Lorentzian fits to the co-/counter-propagating spectra at the minimum power used (168(14) / 58(2) MHz, respectively) approach the predicted 3-level-rate-equation-model linewidths [17] (145 / 55 MHz), further evidence that this experiment cannot resolve the intermediate or excited state hyperfine structure.

The uncertainty for the absolute energy of the $2s3d\,^1D_2$ state is given by the quadrature sum of all uncertainties shown in Table I for a final value of 64 428.40321(55) cm^{-1}, in agreement with and a factor of 180× more precise than the previous experimental result [13]. For the individual $2s^2\,^1S_0 - 2s2p\,^1P_1$ and $2s2p\,^1P_1 - 2s3d\,^1D_2$ transition energies, we conservatively incorporate the possibility that our spectral feature may be dominated by transitions to/from one of the intermediate or excited hyperfine levels by including as well the 37 MHz spectral width observed in our previous $^1P_1$ saturated absorption measurements into our uncertainty budget. We find 42 565.4503(14) cm^{-1} for the $2s^2\,^1S_0 - 2s2p\,^1P_1$ transition, in agreement with our previous measurement of 42 565.4501(13) cm^{-1} [4]. For the $2s2p\,^1P_1 - 2s3d\,^1D_2$ transition energy we find 21 862.9529(14) cm^{-1}, in agreement with and a factor of 36× more precise than the previous experimental result [13].

V. CONCLUSION

This measurement of the absolute energy of the $2s3d\,^1D_2$ state is limited by the unresolved hyperfine structure of the $^1D_2$ state. Both the $2s^2\,^1S_0 - 2s2p\,^1P_1$ and $2s2p\,^1P_1 - 2s3d\,^1D_2$ transitions include an additional uncertainty from the unresolved hyperfine structure of the $2s2p\,^1P_1$ state. Measurements are underway to improve the precision of the $^1P_1$ center-of-gravity energy by performing saturated absorption spectroscopy in a high magnetic field; repeating the resonant two-photon spectroscopy measurement in a high magnetic field would likewise improve the determination of the $^1D_2$ center-of-gravity energy by splitting the currently-merged hyperfine substructure. Repeating the $2s2p\,^1P_1 - 2s3d\,^1D_2$ measurement in a see-through hollow-cathode beryllium lamp would remove the resonant two-photon systematic shifts arising in transverse atomic beam spectroscopy.

The results presented in this paper call for further improvement in the theoretical models. Sharkey *et al.* calculated the absolute energy of the $2s3d\,^1D_2$ state, using ECG, but not including relativistic or QED corrections, to be $64\,418.17(5)$ cm^{-1} [11]. The improved experimental value of $64\,428.40321(55)$ cm^{-1} provides guidance for future calculations, including a test of QED if included in the calculation.

The current uncertainty on the experimental value of the absolute energy of $2s3d\,^1D_2$ state is suitable for future experimental determination of the ionization threshold using Rydberg spectroscopy of the $2s3d\,^1D_2 - 2snp\,^1P$ transitions. This measurement, when compared to the calculated value of $75\,192.699(7)$ cm^{-1} [1], which includes a QED shift of $0.583(5)$ cm^{-1}, will also serve as a test of QED.

[1] M. Puchalski, J. Komasa, and K. Pachucki, Phys. Rev. A **87**, 030502(R) (2013).

[2] M. Stanke, J. Komasa, S. Bubin, and L. Adamowicz, Phys. Rev. A **80**, 022514 (2009).

[3] I. Hornyák, L. Adamowicz, and S. Bubin, Phys. Rev. A **100**, 032504 (2019).

[4] E. C. Cook, A. D. Vira, C. Patterson, E. Livernois, and W. D. Williams, Phys. Rev. Lett. **121**, 053001 (2018).

[5] J. S. Sims and S. A. Hagstrom, J. Chem. Phys. **140**, 224312 (2014).

[6] M. B. Ruiz, F. Latorre, and A. M. Frolov, in *Electron Correlation in Molecules ab initio Beyond Gaussian Quantum Chemistry*, Advances in Quantum Chemistry, Vol. 73, edited by P. E. Hoggan and T. Ozdogan (Academic Press, 2016) pp. 119 – 138.

[7] A. M. Frolov and M. B. Ruiz, Chem. Phys. Lett. **595-596**, 197 (2014).

[8] M. Puchalski, K. Pachucki, and J. Komasa, Phys. Rev. A **89**, 012506 (2014).

[9] A. Krieger, W. Nörtershäuser, C. Geppert, K. Blaum, M. L. Bissell, N. Frömmgen, M. Hammen, K. Kreim, M. Kowalska, J. Krämer, R. Neugart, G. Neyens, R. Sánchez, D. Tiedemann, D. T. Yordanov, and M. Zakova, Appl. Phys. B **123**, 15 (2017).

[10] J. A. Jansen, R. T. Peerdeman, and C. De Vries, Nucl. Phys. **A188**, 337 (1972).

[11] K. L. Sharkey, S. Bubin, and L. Adamowicz, Phys. Rev. A **84**, 044503 (2011).

[12] W. R. Bozman, C. H. Corliss, W. F. Meggers, and R. E. Trees, J. Res. Natl. Bur. Stand. **50**, 131 (1953).

[13] L. Johansson, Ark. Fys. **23**, 119 (1962).

[14] R. Beigang, D. Schmidt, and P. J. West, J. Phys. Colloques **44**, C7 (1983).

[15] M. J. Seaton, J. Phys. B **9**, 3001 (1976).

[16] A. Kramida, Yu. Ralchenko, J. Reader, and and NIST ASD Team, NIST Atomic Spectra Database (ver. 5.7.1), [Online]. Available: `https://physics.nist.gov/asd` [2020, January 7]. National Institute of Standards and Technology, Gaithersburg, MD. (2019).

[17] J. E. Bjorkholm and P. F. Liao, Phys. Rev. A **14**, 751 (1976).

[18] N. F. Ramsey, *Molecular Beams* (Oxford University Press, 1956).

[19] C. Patterson, A. D. Vira, M. T. Herd, W. B. Hawkins, and W. D. Williams, Rev. Sci. Instrum. **89**, 033107 (2018).

[20] J. I. Thorpe, K. Numata, and J. Livas, Opt. Express **16**, 15980 (2008).

[21] R. W. P. Drever, J. L. Hall, F. V. Kowalski, J. Hough, G. M. Ford, A. J. Munley, and H. Ward, Appl. Phys. B **31**, 97 (1983).

[22] R. Salomaa, J. Phys. B **10**, 3005 (1977).

[23] O. Poulsen, T. Andersen, and N. J. Skouboe, J. Phys. B **8**, 1393 (1975).